Dalton Transactions

PAPER

View Article Online
View Journal | View Issue

Check for updates

Cite this: *Dalton Trans.*, 2025, **54**, 13658

Ultramicroporous Al(III) MOFs with selective CO_2 adsorption, acid resistance, and efficient Cr(VI) sorption properties

Dimitrios A. Evangelou,†[a] Eleni C. Makri,†[b] Nikolaos Pliatsios,[c] Ioannis Vamvasakis,[d] Emilia Buchsteiner,[e] Panagiotis Oikonomopoulos,[f] Gerasimos S. Armatas,[d] Giannis S. Papaefstathiou,[f] Theodore Lazarides[c] and Manolis J. Manos*[b]

Received 21st July 2025,
Accepted 12th August 2025

DOI: 10.1039/d5dt01717c

rsc.li/dalton

In the present work, we report the hydrothermal synthesis and detailed characterization of a series of ultramicroporous, luminescent, multivariate metal–organic frameworks (MOFs) with the general formula $[Al(OH)(IATP)_{1-x}(NH_2\text{-}BDC)_x]$, constructed from two different dicarboxylate ligands, H_2IATP = 2-(((1*H*-imidazol-4-yl)methyl)amino) terephthalic acid and NH_2-H_2BDC = 2-aminoterephthalic acid. Structural analysis, using both powder X-ray diffraction (PXRD) and microcrystal electron diffraction (MicroED), confirms that the reported **MTV-Al-MOFs** are topological analogues of the related **NH_2-MIL-53(Al)** MOF. Introducing ultramicroporosity (~5.2 Å) together with bulky imidazole functional groups significantly enhances the chemical stability of these MOFs under acidic conditions, compared to **NH_2-MIL-53(Al)**. It also imparts interesting carbon dioxide physisorption properties, with **MTV-Al-MOF-4** $[Al(OH)(IATP)_{0.39}(NH_2\text{-}BDC)_{0.61}]$ demonstrating a maximum CO_2 adsorption capacity of 2.33 mmol g^{-1} at 273 K and a selectivity CO_2/N_2 of ~76 at the same temperature (273 K) and low-pressure limit. Among the series, **MTV-Al-MOF-4** exhibits the most promising combination of chemical stability and Cr(VI) sorption capacity. This material was extensively studied for eliminating $Cr_2O_7^{2-}$ anions from acidic aqueous solutions, indicating high sorption capacity (174 mg $Cr_2O_7^{2-}$ per g), rapid uptake kinetics (equilibrium reached within 5 minutes), and decent selectivity against competing anions such as Cl^-, NO_3^-, and SO_4^{2-}. For practical applications in wastewater treatment, a MOF-calcium alginate (CA) composite material was fabricated in beads and effectively removed Cr(VI) from diluted electroplating waste under dynamic flow conditions. Finally, all **MTV-Al-MOFs** displayed fluorescence with quantum yields in the range of 4.64–9.53%, while Cr(VI)-loaded **MTV-Al-MOF-4** shows a pronounced reduction in fluorescence quantum yield by a factor of four, thereby confirming the presence of ligand-sorbent interactions leading to photoinduced energy and/or electron transfer processes. Overall, this study highlights a versatile approach to designing multifunctional MOFs with potential applications in environmental remediation, industrial wastewater treatment, luminescence, and gas separation.

1. Introduction

Water, the most abundant natural resource on Earth, is severely threatened due to the accelerated growth of industrial production and urban expansion over the past two decades. This has led to the widespread contamination of aquatic environments, with heavy metal ions being some of the most frequently discharged pollutants.[1–5] The bioaccumulative nature of these metals poses a crucial global concern, threatening both the environment and human health.[1,4–7]

A prime example of such a contaminant in wastewater is chromium, which is released from various activities due to the extensive use of chromium compounds in different industrial

---

[a] Department of Chemistry, Northwestern University, Evanston, Illinois 60208, USA
[b] Department of Chemistry, University of Ioannina, GR-45110 Ioannina, Greece. E-mail: emanos@uoi.gr
[c] Department of Chemistry, Aristotle University of Thessaloniki, GR-54124 Thessaloniki, Greece
[d] Department of Materials Science and Engineering, University of Crete, GR-70013 Heraklion, Greece
[e] Rigaku Europe SE, Hugenottenallee 167, 63263 Neu-Isenburg, Germany
[f] Department of Chemistry, National and Kapodistrian University of Athens, GR-15771 Athens, Greece

† These authors contributed equally to this work.

sectors, including textiles, electroplating, leather tanning, pigments, and ceramics. Chromium typically exists in the oxidation states of Cr(III) and Cr(VI), with Cr(VI) occurring in the form of $Cr_2O_7^{2-}$, $HCrO_4^-$ or CrO_4^{2-}, depending on the Cr concentration and pH levels of the effluents.[8–12] Due to its higher redox potential, water solubility, and cell penetration ability, hexavalent chromium poses more significant hazards than trivalent chromium. Within the body, it creates stable complexes with proteins and nucleic acids, resulting in serious health problems such as stomach ulcers, dermatitis, organ damage, and cancer over long-term exposure.[6,10,13–15]

Various methods have been employed to remediate Cr(VI) and other heavy metals from water, including chemical precipitation, redox reactions, photocatalysis, coagulation–flocculation, membrane/resin separation, ion exchange, and sorption. However, these technologies often face high costs, energy consumption, complexity, secondary pollution, sludge production, and inferior selectivity among other metal ions.[4,12,16–19] Among these strategies, sorption has garnered considerable attention due to its low operating cost, simple design and operation, high efficiency, and potential for regeneration.[8,12,20,21]

Metal–organic frameworks (MOFs), a subgroup of coordination polymers, are crystalline materials composed of organic linkers that coordinate with metal ions or clusters.[22–25] These innovative materials offer significant advantages over conventional sorbents, including vast surface areas, abundant active ion-binding sites, high chemical and hydrothermal stability, and enhanced selectivity. Furthermore, their properties can be finely tuned through post-synthetic modification, enhancing sorption performance. Consequently, MOFs are emerging as the next generation of sorbents for wastewater treatment.[26–30] To date, numerous studies have identified various MOFs with promising heavy metal sorption capabilities,[26,30–34] with the majority focusing on removing CrO_4^{2-} and/or $Cr_2O_7^{2-}$ oxoanions from aqueous media.[8,35–37] The frameworks reported in the literature are primarily cationic, enabling effective anion exchange with Cr(VI) pollutants,[38–43] which can be captured through electrostatic interactions with positively charged amino groups[44–48] or by coordinating with active metal sites.[49–51]

In addition to sorption, which dominates research on the environmental applications of MOFs, the detection and quantification of toxic contaminants are equally significant. In recent years, luminescent metal–organic frameworks (LMOFs), which serve as fluorescent sensing probes for various pollutants, including heavy metals, have garnered considerable attention.[52–56] MOFs' key features—their polymeric structure, well-defined chemical environment, and inherent porous structure—offer improved sensitivity and selectivity toward target analytes compared to most conventional chemical sensors.[52,53,57–59] Frameworks displaying efficient fluorescence and the ability to sorb Cr(VI) oxoanions show significant potential for luminescence-based sensing applications. Amino-decorated materials are particularly promising for designing functional LMOFs, as the amino group exhibits strong anion-binding properties and facilitates electron transfer with the oxoanionic species acting as an electron-donating group.[51,60–62] Therefore, significant efforts have been made to develop new multifunctional amino-decorated luminescent-sensing MOFs.

Ultramicroporous metal–organic frameworks (Um-MOFs), defined as MOFs with pore sizes lower than 0.7 nm,[63–65] could be interesting candidates for applications in the sensing and sorption of water pollutants. Um-MOFs would be of great interest for such applications since their small pore sizes may enhance MOF–pollutant interactions and the robustness of the materials' structures. Although Um-MOFs have been extensively studied for their gas sorption and separation properties,[66–73] little attention has been paid to their potential use in water treatment and sensing.[74–76]

Following our previous work on a multifunctional Al(III)-MOF termed **Al-MOF-1**,[43] we synthesized a terephthalate ligand with alkyl-amino-imidazole functional groups, namely $IATP^{2-}$ = 2-(((1*H*-imidazol-4-yl)methyl)amino)terephthalate, targeting MOFs with an increased number of sorption sites (*i.e.*, nitrogen-containing groups) interacting strongly with Cr(VI) anions. Although this was not our initial intention, we expanded our research efforts toward ultramicroporous and multivariate materials[77–81] to achieve microporosity and optimize both the sorption capacity and stability of the new sorbents.

Herein, we report a series of ultramicroporous, multivariate Al^{3+}-MOFs (**MTV-Al-MOFs**), with the general formula $[Al(OH)(IATP)_{1-x}(NH_2\text{-BDC})_x]\cdot$solvent (**MTV-Al-MOF-1**, $x = 0.30$; **MTV-Al-MOF-2**, $x = 0.44$; **MTV-Al-MOF-3**, $x = 0.56$; **MTV-Al-MOF-4**, $x = 0.61$; and **MTV-Al-MOF-5**, $x = 0.70$; $NH_2\text{-BDC}^{2-}$ = 2-aminoterephthalate). The new materials belong to the family of MIL-53 MOFs, as demonstrated *via* electron diffraction and powder X-ray diffraction studies. They display remarkable stability in acidic aqueous media, unlike the related **NH_2-MIL-53(Al)**. Considering that industrial Cr(VI) waste streams are highly acidic ($pH \leq 3$),[82,83] the new MOFs, which combine acid stability and a positive surface charge, seem promising sorbents for hexavalent chromium. Certainly, **MTV-Al-MOF-4**, the most promising material among the multivariate MOFs, exhibits rapid sorption kinetics, achieving equilibrium in only 5 minutes of contact time and a highly efficient sorption capacity of approximately 174 mg $Cr_2O_7^{2-}$ per g. In addition, its Cr(VI) sorption performance is retained high even in the presence of competitive species in significant excess. Furthermore, mm-sized beads of the activated **MTV-Al-MOF-4** were isolated using the calcium alginate-encapsulation method.[84] Notably, the beads mixed with sea sand were used to remove hexavalent chromium from acidic industrial waste under continuous flow conditions, and the results were encouraging, with a significant amount of Cr(VI) waste decontaminated as it passed through the MOF-CA beads. Additionally, the photophysical properties of the MOFs were studied in detail, revealing their strong luminescence. Fluorescence studies on Cr-free and Cr-loaded **MTV-Al-MOF-4** reveal that the sorption of Cr(VI) leads to a significant reduction in fluorescence quantum yield. The quantum yield decreases by a factor of four, from 4.6 to 1.1%. Interestingly, the average fluorescence lifetime decreases less dramatically, from 3.7 to 2.5 nanoseconds, pointing toward a predominantly static quenching mechanism. Furthermore, the **MTV-Al-MOFs** demonstrated selective CO_2 *versus* N_2 adsorption, broadening the potential fields of application for these multivariate materials. Overall, this study highlights the multifunctionality of the new ultramicroporous MIL-53(Al) multivariate analogs, demonstrating their effectiveness in capturing and detecting Cr(VI) under acidic conditions, as well as their potential for selective gas sorption and separation processes.

2. Results and discussion

2.1. Synthesis and structural characterization of MTV-Al-MOF-1

As noted in the introduction, a recent study of ours[44] demonstrated that incorporating a pyridine-functionalized aminoterephthalate linker yielded an exceptionally effective and robust heavy metal sorbent, primarily due to bulky, nitrogen-rich functionalities. Additionally, the aromatic backbone imparted interesting photophysical properties to the MOF, broadening its potential applications as a photoluminescent sensing probe. Therefore, to design improved MIL-53 multifunctional analogs, we investigated the chemistry of Al^{3+} ions with a newly synthesized imidazole-decorated dicarboxylate ligand (see SI), which features several amino binding sites for the harmful Cr(VI) oxoanions.

The **MTV-Al-MOF-1** material was obtained with high purity and crystallinity *via* a solvothermal reaction of $AlCl_3{\cdot}6H_2O$ and a new ligand H_2IATP, or 2-(((1*H*-imidazol-4-yl)methyl)amino) terephthalic acid (Fig. 1a and S1), in H_2O/DMF (9 : 1 v/v) using a Parr stainless-steel autoclave at 120 °C. Various mixtures of *N*,*N*-dimethylformamide (DMF) and deionized water were studied over various temperatures to identify the optimal conditions for ensuring phase purity, reproducibility, and yield.

Unfortunately, the new material was isolated in the form of microcrystalline powder. Thus, microcrystal electron diffraction (MicroED) and powder X-ray diffraction (PXRD) were applied to determine and refine its structural features. The MicroED data indicated that the Al^{3+}-MOF crystallizes in the orthorhombic space group *Imma* (no. 74) ($a = 17.54(9)$, $b = 6.77(10)$, $c = 12.74(15)$ Å and $V = 1514(29)$ Å^3) and displays topological characteristics similar to other members of the MIL-53 family. It specifically demonstrates the characteristic ***sra*** topology, which relates to a rod net architecture consisting of one-dimensional [–(OH)–M–] rods as secondary building units (SBUs), where M represents Al^{3+}, Cr^{3+}, *etc.*[85] The 3D structure of **MTV-Al-MOF-1**, along with a diffraction image of a microcrystallite, is shown in Fig. 1b and c. The side groups could not be located due to significant disorder and the limitations of the ED method. Nevertheless, the overall structural connectivity, as determined from the data, is without doubt. Selected crystal data for **MTV-Al-MOF-1** are given in Table S1. In Fig. 1d, a structural model of the compound, including the side groups of the linkers, is shown. We should also note that the structural model includes mixed NH_2-BDC^{2-} and $IATP^{2-}$ ligands, with a ratio of NH_2-BDC^{2-}/$IATP^{2-}$ (25/75) roughly the experimental ratio for **MTV-Al-MOF-1** (30/70). Although this is not an accurate structural model of **MTV-Al-MOF-1**, it is useful for the visualization of the functional groups of the ligands.

As shown in Fig. 2a, the PXRD data for the new MOF align well with the diffraction pattern theoretically generated from the crystallographic data. The PXRD data of **MTV-Al-MOF-1** were successfully indexed in the orthorhombic crystal system

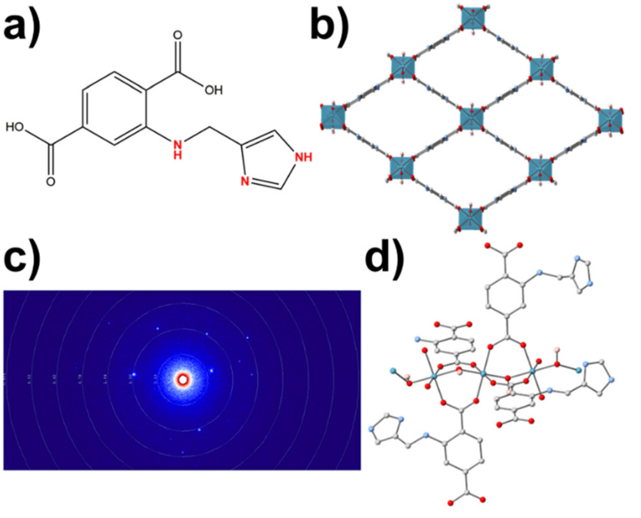

Fig. 1 (a) Illustration of the H_2IATP ligand. (b) The 3D structure of **MTV-Al-MOF-1**, viewed along the *b*-axis as determined by MicroED data, which is constructed by the connection of parallel inorganic chains of octahedrally coordinated metal centers [$Al^{3+}O_4(OH)_2$] and $IATP^{2-}$ linkers (Al: Turquoise octahedra, O: red, C: grey, N: blue. H atoms were omitted for clarity). N atoms are positionally disordered over four positions. The side $-CH_2-$Imidazole groups could not be located. (c) An electron diffraction (ED) image of a microcrystallite of **MTV-Al-MOF-1**. (d) A structural model, derived from the structure determined from MicroED, which was built and optimized with Avogadro.[86]

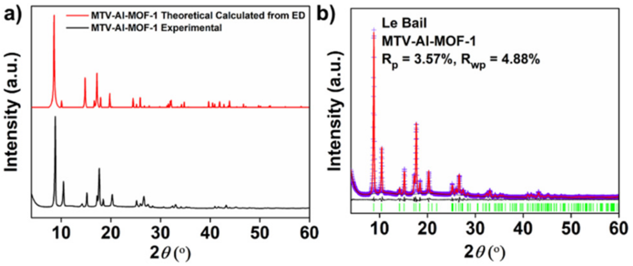

Fig. 2 (a) Comparison between the experimental powder diffraction pattern of **MTV-Al-MOF-1** and the theoretically derived diffraction pattern based on the ED data. (b) Le Bail plot of **MTV-Al-MOF-1**. Violet crosses: experimental points; red line: calculated pattern; black line: difference pattern (exp. − calc.); green bars: Bragg positions. Space group: *Imma* (no. 74). Cell parameters: $a = 16.976(5)$, $b = 6.623(2)$, $c = 12.508(4)$ Å and $V = 1406.4(8)$ Å^3.

with *Imma* space group. A structureless (Le Bail) refinement,[87,88] further confirmed these findings and the high purity of the new material (Fig. 2b).

Nuclear magnetic resonance (NMR) studies were conducted for **MTV-Al-MOF-1** in a highly alkaline D_2O solution to further assess the molecular integrity of the new ligand within the framework. The ^1H NMR measurement confirmed the successful incorporation of the H_2IATP ligand, as evidenced by all the distinctive signals (Fig. S2). Nonetheless, additional peaks were also observed, accounting for approximately 30% of NH_2-BDC^{2-} ligands (Fig. S2). This indicates a significant loss of alkyl chains, likely due to partial ligand decomposition during the MOF's synthesis. Although our original purpose was to synthesize the MIL-53 analog using the new H_2IATP ligand, we isolated a multivariate MOF with a ratio of approximately 2.33 for $IATP^{2-}$/NH_2-BDC^{2-}. As a result, we decided to shift our focus toward synthesizing a variety of multivariate frameworks.

2.2. Synthesis and structural characterization of ultramicroporous MTV-Al-MOFs

Our efforts to isolate multivariate MOFs based on two different dicarboxylate linkers, *i.e.*, H_2IATP and NH_2-H_2BDC, were initiated by exploring various ligand ratios while maintaining identical reaction conditions and solvent systems as those used in the case of **MTV-Al-MOF-1** (see SI). Integrating these distinct organic ligands enables the synthesis of sorbent materials with enhanced performance. The presence of imidazole rings contributes to improved hydrolytic and chemical stability, whereas the unsubstituted NH_2-BDC^{2-} linkers provide accessible voids, facilitating the formation of MOFs with ultramicroporosity. This structural combination, guided by the chosen ligand ratio, can significantly improve specific properties of the resulting MOFs.

To our delight, we successfully isolated four new crystalline **MTV-Al-MOFs** (designated as **MTV-Al-MOF-2** through **MTV-Al-MOF-5**) in high yield and phase purity. PXRD studies confirmed that all the synthesized multivariate frameworks are topological analogs of **MTV-Al-MOF-1** (***sra*** topology), showing insignificant structural differences as the NH_2-H_2BDC percentage increased (Fig. 3). The PXRD data for all four new **MTV-Al-MOFs** were accurately indexed to the orthorhombic crystal system with the *Imma* space group. Their unit cell parameters were refined by applying the Le Bail analysis (Fig. S3–S6). For reference, the parent material **NH_2-MIL-53(Al)** was synthesized following the experimental route outlined in the SI.

The actual structural composition of every **MTV-Al-MOF** was determined using NMR spectroscopy (Fig. S7–S10). By integrating the characteristic signals for 2-(((1*H*-imidazol-4-yl)methyl)amino)terephthalic acid and 2-aminoterephthalic acid, the following $IATP^{2-}$/NH_2-BDC^{2-} ratios were calculated: 1.27, 0.79, 0.64, and 0.43 for **MTV-Al-MOF-2**, **MTV-Al-MOF-3**, **MTV-Al-MOF-4**, and **MTV-Al-MOF-5**, respectively. The observed ratios slightly deviate from those initially selected for the reaction mixtures, with the discrepancy likely stemming from partial degradation of the imidazole-decorated ligand during the self-assembly process. This decomposition effect has been previously pointed out in the case of **MTV-Al-MOF-1**. Consequently, the actual ratios reflect a slight increase in the proportion of 2-amino terephthalate. The sharp peaks observed at around 2.1 ppm and 8.3 ppm in all the ^1H NMR spectra of the as-synthesized MOFs (Fig. S2, S7–S10) can be attributed to dimethylamine ($(CH_3)_2NH$) and formate anions ($HCOO^-$) signals, respectively. These species result from the basic hydrolysis of DMF within the framework. Both hydrolyzed and unhydrolyzed DMF were considered in estimating the total DMF content.[44]

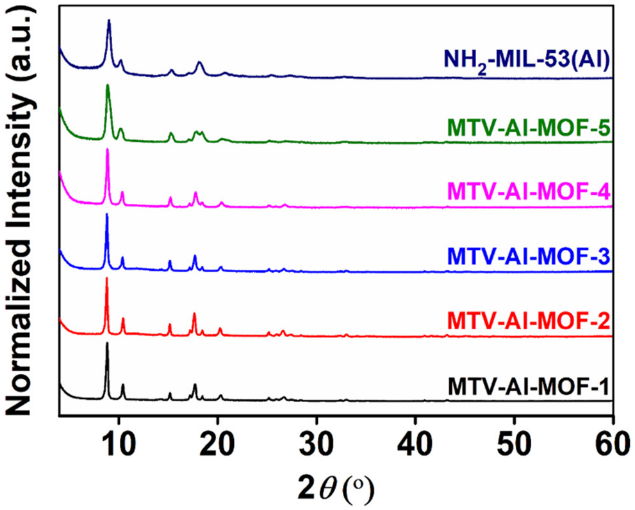

Fig. 3 PXRD data comparing the various **MTV-Al-MOFs** and **NH_2-MIL-53(Al)**.

2.3. Chemical stability studies for MTV-Al-MOFs

Hexavalent chromium waste streams are typically acidic;[82] therefore, we next evaluated the chemical stability of the new **MTV-Al-MOFs** and the parent material, **NH_2-MIL-53(Al)**, under acidic conditions at pH 3 and 10 minutes of contact time. The contact time was selected based on the values (5–10 min) used in the sorption studies, see below. PXRD analysis (Fig. 4) confirmed that the structural integrity of the frameworks was fully retained up to **MTV-Al-MOF-4**. In contrast, a partial loss of crystallinity was observed in **MTV-Al-MOF-5** (Fig. 4), which exhibits the lowest ratio of $IATP^{2-}$ to NH_2-BDC^{2-} ligands, as evidenced by the broader diffraction peaks in the PXRD pattern of this material. Comparatively, **NH_2-MIL-53(Al)** exhibited a substantial loss of crystallinity following short-term exposure to the acidic aqueous solution (Fig. 4). **NH_2-MIL-53(Al)** is highly porous, making the framework more vulnerable to damage by reactive species, such as H^+. On the contrary, **MTV-Al-MOFs** incorporate a significant fraction of relatively bulky –NH–CH_2–Im groups, which likely shield the Al^{3+} metal sites from attack by various species. Hence, **MTV-Al-MOF-4** emerges as the most promising candidate among these MOFs, offering exceptional chemical robustness and the highest possible NH_2-BDC^{2-} linker content. Besides being stable in acidic solutions, **MTV-AL-MOF-4** is also stable under alkaline con-

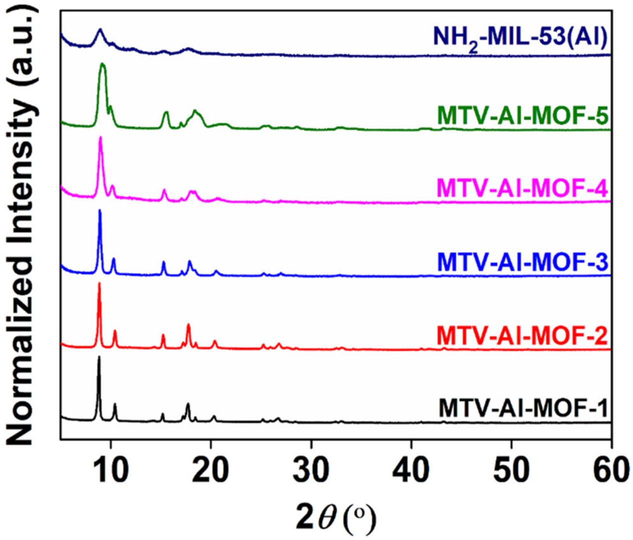

Fig. 4 Comparative PXRD data for the various **MTV-Al-MOFs** and **NH_2-MIL-53(Al)** following treatment with an acidic aqueous solution of pH 3 for 10 minutes.

ditions (Fig. S11). These properties establish **MTV-Al-MOF-4** as a promising sorbent for efficiently removing Cr(VI) from harsh aqueous environments.

2.4. Additional characterizations

The attenuated total reflectance infrared spectroscopy (ATR-IR) measurements for all the multivariate MIL-53(Al) MOFs are presented in Fig. S12–S16. All ATR-IR spectra display characteristic absorption peaks associated with the functional groups of the two distinct terephthalate substituents. More specifically, IR peaks ranging from 3488 to 3498 cm^{-1} and 3376 to 3380 cm^{-1} are assigned to the stretching vibrations of the N–H bond of primary amine groups (NH_2-BDC^{2-}) and secondary amine groups (originating from the aliphatic and imidazolate amino moieties), respectively. We can observe that the intensity of the $-NH_2$ signal is enhanced along with the decrease of the $IATP^{2-}$/NH_2-BDC^{2-} ligand ratio (Fig. S12–S16). Peaks around 2900 and 1438 cm^{-1} are attributed to the stretching and bending vibrations of the C–H bond in the aliphatic methylene group ($-CH_2-$), respectively. Additionally, the characteristic IR peak corresponding to the stretching vibration of the C=O bond of DMF is recorded at 1666 cm^{-1}, owing to the free solvent molecules located either on the external surface or inside the pores of the frameworks.[89,90] The intensity of this signal appears to be enhanced for the **MTV-Al-MOFs** with a lower ratio of $IATP^{2-}$ to NH_2-BDC^{2-} (Fig. S17). The presence of DMF species was already validated by ^1H NMR (Fig. S2 and Fig. S7–S10). The two sharp IR peaks, attributed to the asymmetric and symmetric stretching vibrations of carboxylate groups, are recorded at 1572–1580 cm^{-1} and 1394–1398 cm^{-1}, respectively, with a difference of $\Delta\nu(COO^-)$ ~178–182 cm^{-1}. This value indicates the presence of bridging carboxylates.[91] Finally, the stretching vibration of the aromatic rings' double carbon bond (–C=C–) is observed around 1505 cm^{-1}. In addition, field-emission scanning electron microscopy (FE-SEM) revealed that the new multivariate MOFs consist of microcrystallites with different morphologies and sizes smaller than 5 μm (Fig. S18–S22). Energy-dispersive X-ray spectroscopy (EDS) indicated the presence of chloride in MOFs (Fig. S23–S27). The Cl^- anions are present as HCl and formed through the *in situ* hydrolysis of the aluminum salt. This HCl may be firmly bound to the surface of the particles through electrostatic interactions. The Al to Cl atomic ratio ranged from 9.9 to 15.8 for all **MTV-Al-MOFs**. Based on the DMF and HCl content determined from EDS and ^1H NMR analyses, we estimated the full chemical composition of the pristine **MTV-Al-MOFs**. Thermogravimetric analysis (TGA) data were collected for this purpose. As shown in Fig. S28, the differential thermogravimetric (DTG) curve of **MTV-Al-MOF-4** exhibits three distinct weight loss steps, consistent with the expected thermal decomposition behavior. The first weight loss of 2.48% occurs between room temperature and 73 °C and likely results from the release of weakly bound lattice water molecules. The second weight loss of 17.62% up to 280 °C is attributed to the removal of firmly bound water, DMF, and HCl. The final and most significant weight loss of 52.06% occurs up to 600 °C and corresponds to the thermal decomposition of the framework through the release of organic substituents. Similar observations were made for the remaining multivariate MOFs (Fig. S29–S32). Total solvent removal is assumed to occur at 280 °C. Using this assumption and the observed weight loss data, we calculated the H_2O content to be 0.70 mol of H_2O per mol of as-synthesized **MTV-Al-MOF-4** (see SI). Applying the same method, we estimated the water content of the other pristine **MTV-Al-MOFs**, which ranged from 0.05 to 1.87 mol H_2O per mol of MOF.

2.5. Preparation and characterization of the activated MTV-Al-MOFs

Before Cr(VI) sorption studies in acidic media, all synthesized MOFs underwent activation. This process was carried out in two different steps: (i) solvent exchange using ethanol under reflux conditions and (ii) protonation *via* treatment with an aqueous HCl solution at pH 3 (details provided in the SI). This activation procedure was crucial for fully protonating the imidazole and amino functionalities and removing guest solvent molecules, unreacted ligands, and other precursors from the pores. As a result, the materials offered both accessible pore channels and surface-active sites to promote interactions with Cr(VI) oxoanions.

PXRD analysis and Le Bail refinements revealed that the crystal structure of activated **MTV-Al-MOFs** remains intact after the activation procedure (Fig. S33–S38). The ^1H NMR data (Fig. S39–S43), collected after digesting the activated MOFs in a highly alkaline D_2O solution, revealed the successful removal of the DMF molecules, as well as insignificant variations in the $IATP^{2-}$/NH_2-BDC^{2-} fractions. The ratio values determined for the activated **MTV-Al-MOFs** were 2.13, 1.44, 0.82, 0.64, and 0.45 for **MTV-Al-MOF-1**, **MTV-Al-MOF-2**, **MTV-Al-MOF-3**,

MTV-Al-MOF-4, and **MTV-Al-MOF-5**, respectively. In comparison, the corresponding values for the pristine materials were 2.33, 1.27, 0.79, 0.64, and 0.43, respectively. A significant proportion of DMF is eliminated during the activation process, as confirmed by ^1H NMR measurements (Fig. S39–S43). However, some amounts of residual DMF remain. Specifically, the estimated DMF removal percentages following activation were 60%, 64%, 61%, 77%, and 79% for **MTV-Al-MOF-1** through **MTV-Al-MOF-5**, respectively. Most formic acid observed in the ^1H NMR spectra of the activated **MTV-Al-MOFs** results from the decomposition of DMF during the thermal activation process.[92] Only a small amount of dimethylamine ($(CH_3)_2NH$) and a minor fraction of formic acid are generated through the basic hydrolysis of DMF throughout sample preparation. The remaining DMF and formic acid molecules are likely strongly adsorbed on external surfaces or trapped within less accessible regions of the framework, making their removal more difficult. Additionally, ATR-IR studies (Fig. S44–S48) showed no considerable alterations in the spectra of the activated materials compared to the pristine samples, except for the loss of the characteristic DMF vibrational peak, further validating the high effectiveness of the activation process. FE-SEM imaging confirmed that the morphology and size of the MOF particles remained generally similar after activation (Fig. S18–S22). EDS analysis (Fig. S49–S53) indicated the presence of Cl in the activated materials, attributed to the positively charged surface, which is essential for capturing Cr(VI). Indeed, the zeta potential for the activated **MTV-Al-MOF-4**, the most promising Cr(VI) sorbent among all reported **MTV-Al-MOFs**, was +46.5 mV at pH ~7 (Fig. S54d). The rest of the reported MOFs also exhibited similar positive surface charges under neutral conditions, with ζ-potential values ranging from +45.4 to +52.1 mV (Fig. S54). The variation in $IATP^{2-}/NH_2\text{-}BDC^{2-}$ ratios showed no systematic effect on the ζ-potential values. The thermal behaviour of the materials was also studied using thermogravimetric analysis (TGA) (Fig. S55–S59). Three distinct weight loss stages are observed in the differential (DTG) graph of the activated **MTV-Al-MOF-4** (Fig. S55b). The first weight loss of 3.34% occurs from room temperature to 110 °C and is attributed to the release of solvent molecules, primarily water. This is followed by a second weight loss of 2.67% up to 210 °C, attributed to the removal of firmly bound water, residual DMF, formic acid and HCl. The final weight loss of 72.24% occurs up to 650 °C, corresponding to the decomposition of the framework's structure by releasing organic ligands. A similar behaviour was observed for the other **MTV-Al-MOFs** (Fig. S56–S59). As with the as-synthesized **MTV-Al-MOFs**, we utilized the TGA data to estimate the water content of the activated **MTV-Al-MOF-4**, assuming complete solvent removal occurs at 210 °C. Based on this assumption and the observed weight loss data, we calculated the H_2O content to be 0.37 mol of H_2O per mol of activated **MTV-Al-MOF-4** (see SI). Following the same approach, we estimated the water content of the other activated **MTV-Al-MOFs**, which ranged from 0.12 to 0.44 mol of H_2O per mol of MOF. We should note that TGA analysis cannot be reliably used to calculate the aluminum content (% Al) since the residues proved to be amorphous, and their chemical composition cannot be determined, making comparison with theoretical values not feasible.

2.6. Gas adsorption measurements

Nitrogen physisorption experiments conducted at 77 K (Fig. S60) for the activated samples revealed negligible porosity for all **MTV-Al-MOFs**, with Brunauer–Emmett–Teller (BET) surface areas ranging from 8.3 to 31.5 $m^2\ g^{-1}$. The materials' limited N_2 adsorption capacity likely arises from the bulky $–NH–CH_2–Im$ moieties, which may orient toward the pores, reducing the available void space and hindering molecular diffusion. The side chains of $IATP^{2-}$ ligand may also induce the formation of restricted pore environments (<4 Å) that are not effectively probed by N_2 adsorption. On the contrary, CO_2 adsorption isotherms recorded up to 1 bar at 273 K showed notable adsorption capacities of 0.85, 1.53, 1.71, 2.33, and 1.45 mmol g^{-1} for **MTV-Al-MOF-1** up to **MTV-Al-MOF-5**, respectively (Fig. S61), demonstrating that these multivariate materials exhibit relatively high performance for CO_2 capture. The apparent BET surface areas of **MTV-Al-MOFs**, calculated from CO_2 adsorption isotherms, range from 174 to 300 $m^2\ g^{-1}$ (Fig. S61). Analysis of the single-component adsorption isotherms of CO_2 and N_2 at 273 K and 298 K (Fig. 5a), utilizing ideal adsorption solution theory (IAST),[93] revealed that **MTV-Al-MOF-4** exhibits highly selective CO_2 adsorption over N_2. At 273 K, the CO_2 maximum uptake reached 2.33 mmol g^{-1}, significantly higher than the 0.25 mmol g^{-1} observed for N_2, corresponding to a CO_2/N_2 selectivity factor of approximately 76 in the low-pressure limit (Fig. 5b). Importantly, relatively high selectivity is maintained at ambient temperature, with a CO_2/N_2 selectivity factor of ~38 (Fig. 5b), and CO_2 and N_2 adsorption capacities of 1.23 and 0.19 mmol g^{-1}, respectively (Fig. 5a). Furthermore, analysis of the CO_2 adsorption isotherms using non-local density functional theory (NLDFT) indicates that all **MTV-Al-MOFs** possess ultramicroporous structures with pore sizes of ~5.2 Å (Fig. S62–S66). One likely explanation for the enhanced CO_2 uptake of the **MTV-Al-MOFs** compared to N_2 is their ultramicroporous channel structure, which appears to amplify host–guest interactions. The small

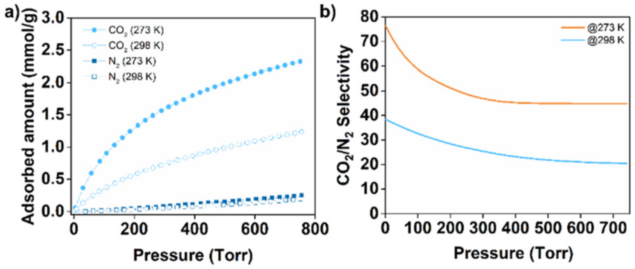

Fig. 5 (a) Adsorption isotherms for CO_2 and N_2 of activated **MTV-Al-MOF-4** at 273 and 298 K. (b) The CO_2/N_2 selectivity predicted using ideal adsorption solution theory (IAST) based on the single-component isotherms at 273 and 298 K for a CO_2/N_2 gas mixture (15 : 85) over activated **MTV-Al-MOF-4**.

pore channels enable these MOFs to discriminate gases based on subtle differences in kinetic diameter (3.3 Å for CO_2 *vs.* 3.64 Å for N_2). Moreover, CO_2, unlike N_2, has a significant quadrupole moment, facilitating strong electrostatic interactions with polar fragments or metal sites within the framework.[94] Thus, the combination of ultramicroporosity and steric hindrance from the bulky imidazole groups plays a crucial role in enhancing these MOFs' gas separation properties and acidic stability.

2.7. Preliminary Cr(VI) sorption study for MTV-Al-MOFs

The developed multivariate MOFs, designed with multiple binding sites and enhanced stability in acidic conditions by incorporating two distinct substituents into their organic backbone, show great potential for capturing the highly harmful $Cr_2O_7^{2-}$ oxoanions. We performed a preliminary batch sorption investigation to identify the most effective sorbent among these materials. These tests utilized a highly concentrated Cr(VI) solution at pH 3, with a V/m ratio of 1 g L^{-1}. The experiments were conducted at room temperature and a contact time of 5 minutes. The UV-Vis spectroscopy analysis of the diluted solutions demonstrated that the activated **MTV-Al-MOF-4** had the highest sorption capacity, reaching up to 180 mg of $Cr_2O_7^{2-}$ per gram of sorbent (Fig. S67). In comparison, **MTV-Al-MOF-1** and **MTV-Al-MOF-3** showed slightly lower sorption capacities, while **MTV-Al-MOF-2** and **MTV-Al-MOF-5** were only 50% as effective as **MTV-Al-MOF-4** (Fig. S67). This trend in sorption efficiency can be explained by examining the crystallite particle sizes of the reported materials, which were calculated using the Scherrer equation (see SI). **MTV-Al-MOF-4** has the smallest particle size (234 nm), compared to those of **MTV-Al-MOF-1** (276 nm), **MTV-Al-MOF-2** (278 nm), and **MTV-Al-MOF-5** (246 nm). Smaller crystallite sizes are associated with a larger external surface area and shorter diffusion pathways, which enhance sorption efficiency. Although **MTV-Al-MOF-3** has an even smaller particle size of 197 nm compared to **MTV-Al-MOF-4**, its slightly lower sorption capacity may result from minor variations in the materials' crystallinity. Based on these findings, we further explored the Cr(VI) sorption properties of **MTV-Al-MOF-4**.

2.8. Cr(VI) batch sorption studies for activated MTV-Al-MOF-4

2.8.1. Sorption kinetics. The sorption studies were primarily conducted at low pH levels (~3), as Cr(IV) waste is typically acidic.[82] The first step of the detailed sorption investigation involved kinetic studies. Initially, we checked the sorption with a Cr(VI) solution (pH ~3) of relatively low concentration (0.795 ppm). Within only 5 min, ~94% Cr(VI) removal was found (Fig. S68), with the final Cr(VI) concentration being ~48 ppb, *i.e.*, below the acceptable limit for Cr(VI) in drinking water (50 ppb).[95] Due to the exceptionally rapid Cr(VI) sorption for such low initial Cr(VI) concentrations, leading to final concentrations in the ppb level, a reliable fitting of the kinetics sorption data is difficult. Therefore, we performed kinetic sorption studies with a much higher Cr(VI) concentration (22 ppm $Cr_2O_7^{2-}$), Fig. 6a. The material was once more an exceptionally fast and efficient sorbent for Cr(VI), with equilibrium reached within only 5 minutes of contact time. The rapid nature of the process is mainly attributed to the strong electrostatic forces between the positively charged surface of **MTV-Al-MOF-4** (protonated amino moieties) and the negatively charged $Cr_2O_7^{2-}$. Further increases in contact time had a negative impact on the removal efficiency. The $Cr_2O_7^{2-}$ sorption by **MTV-Al-MOF-4** is better described by Lagergren's first-order equation (Fig. 6a). This finding aligns with the expected behavior of the material, as physisorption-driven adsorption processes are typically well described by the pseudo-first-order model. Such processes are generally associated with weak interactions, including electrostatic interactions, van der Waals forces, and hydrogen bonding. In contrast, the pseudo-second-order model is more suitable for systems where chemisorption dominates and involves stronger interactions, typically those involving covalent or electron-sharing bonds.[96–98] A later section presents a more detailed discussion regarding the proposed Cr(VI) sorption mechanism.

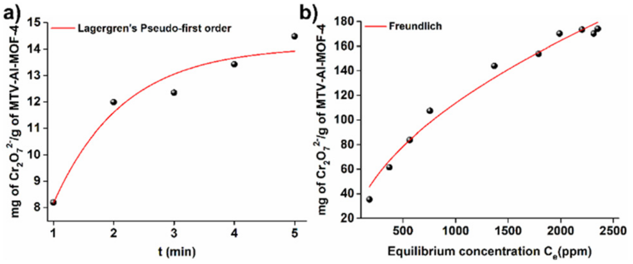

Fig. 6 (a) Fitting of the $Cr_2O_7^{2-}$ kinetics data for **MTV-Al-MOF-4** with Lagergren's first-order equation (initial $Cr_2O_7^{2-}$ concentration ~22 ppm, pH = 3. $R^2 = 0.94$, $q_e = 14.11 \pm 0.48$ mg g^{-1}, $K_L = 0.86 \pm 0.11$ g mg^{-1} min^{-1}). (b) Fitting of the $Cr_2O_7^{2-}$ isotherm data at pH = 3 for **MTV-Al-MOF-4** with Freundlich's model. ($R^2 = 0.98$, $K_F = 2.85 \pm 0.75$ g L^{-1}, $n = 1.87 \pm 0.13$).

2.8.2. pH-dependent sorption studies. The impact of pH on Cr(VI) removal by **MTV-Al-MOF-4** was also investigated using contaminated solutions with varying pH levels, specifically within the pH range of 3 to 9, based on the chemical stability of the sorbent. The sorption results demonstrated the outstanding performance of the new MOF, achieving removal efficiencies of 92% or higher across both acidic and alkaline conditions (Fig. S69). Exceptionally, this MOF showed remarkable effectiveness in acidic conditions (pH = 3–4), with removal rates reaching up to 96.2% (Fig. S69).

2.8.3. Sorption isotherm studies. Analyzing the sorption equilibrium isotherm is essential for assessing the maximum sorption capacity of the sorbent and gaining a deeper understanding of the interactions between the sorbate and sorbent. The Cr(VI) sorption isotherm (pH = 3) for **MTV-Al-MOF-4** is shown in Fig. 6b. The sorption data align very well with the Freundlich isotherm model, and the maximum experimental sorption capacity reaches up to 174 mg of $Cr_2O_7^{2-}$ per g of **MTV-Al-MOF-4** (Fig. 6b). The significant correlation with the Freundlich isotherm model suggests that the sorption process is probably multilayered and occurs within a heterogeneous surface, where physisorption may be the primary mechanism. This finding aligns with the kinetic data and is characteristic of systems exhibiting a non-uniform distribution of active sites.[99,100]

2.8.4. Effect of competitive species. Another critical factor affecting the efficiency of a sorbent in capturing toxic species from wastewater is the presence of competing anions. Cr(VI)-contaminated wastewater often contains various anions at relatively high concentrations.[101,102] Therefore, we next evaluated the ability of **MTV-Al-MOF-4** to remove Cr(VI) in the presence of common anionic competitors, including Cl^-, NO_3^-, SO_4^{2-}, and HPO_4^{2-}. In this study, we selected a relatively low Cr(VI) concentration of 700 ppb to reflect better the levels typically found in actual waste streams. Spectroscopic analysis revealed that **MTV-Al-MOF-4** retains its sorption capability toward $Cr_2O_7^{2-}$, achieving a removal efficiency of 87.6% even in the presence of a 10-fold excess of Cl^- anions (Fig. S70). However, as the Cl^- molar concentration increases to 100 and 1000 times that of Cr(VI), the sorbent's performance declines to 49.2% and 12%, respectively (Fig. S70). The sorption data further indicate that Cr(VI) removal remains unaffected by a 10 and 100-fold excess of NO_3^- anions, with removal efficiencies of 96.1% and 89.1%, respectively (Fig. S70). Additionally, the material maintains remarkable performance in the presence of SO_4^{2-} oxoanions, achieving a 96.3% removal efficiency even with a 10-fold excess (Fig. S70), despite the higher negative charge of sulfate's oxygen atoms (negative charges for sulfate and dichromate oxygen atoms calculated *via* NBO analysis are −1.110 and −0.548 to −0.430, respectively).[44] On the contrary, the sorption efficiency decreases significantly in the presence of HPO_4^{2-} anions (Fig. S70). This effect was anticipated due to the extremely high negative charge density of HPO_4^{2-} oxygen atoms (negative charge of hydrogen phosphate oxygen atoms calculated *via* NBO analysis is −1.300 to −1.067).[44] A higher negative charge strengthens the electrostatic interactions, leading to a stronger preference of **MTV-Al-MOF-4** for these anions.

2.9. Column sorption studies with industrial wastewater samples

In previous studies reported by our group, various MOFs, either in pure composite form with alginate or mixed with silica sand, were implemented as stationary phases in column experiments.[51,84,103,104] In this work, we prepared mm-sized **MTV-Al-MOF-4**/calcium alginate (CA) beads with approximately 89% MOF content. These beads were used as the stationary phase, along with sea sand, in a borosilicate column with an internal diameter of 0.7 cm (beads-to-sand mass ratio = 1 : 10) (Fig. S71). The column, operating in down-flow mode at a flow rate of 2 mL min^{-1}, was employed to treat industrial chrome-plating wastewater containing approximately 170 ppb of Cr(VI). A peristaltic pump was also incorporated into the setup to ensure a steady flow (Fig. S71). Samples of 100 mL were passed through the column and collected in glass beakers. As illustrated in Fig. 7, the Cr(VI) concentration in the effluents was reduced to below 50 ppb (the WHO-defined upper limit for Cr(VI) in drinking water)[95] even after treating 500 mL of diluted industrial wastewater. We should note that this is the first example of Al(III) MOF studied for removing Cr(VI) under flow conditions. Unfortunately, the sorbent's reusability is limited. In cases of non-reusable sorbents, we have proposed recycling the most expensive component of the MOF, namely the organic ligands.[44]

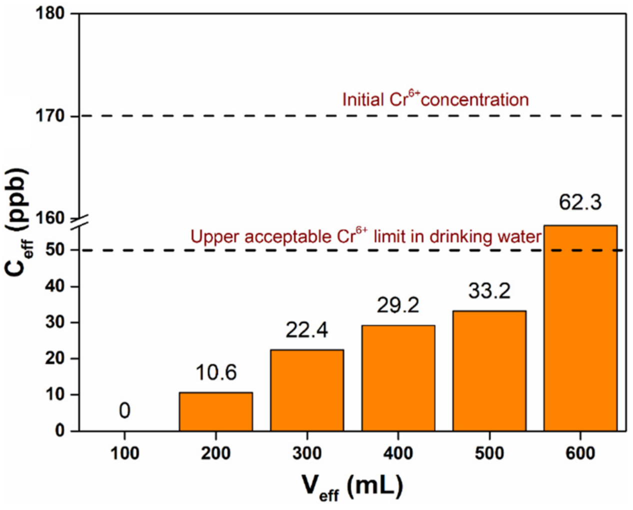

Fig. 7 Column sorption data with chrome-plating wastewater sample (flow rate 2 mL min^{-1}) containing 170 ppb of Cr(VI). V_{eff} and C_{eff} are the volume (mL) and Cr(VI) concentration (ppb) of the solution passed through the column setup (*i.e.*, effluent), respectively.

2.10. Recovery and reuse of organic ligands

As mentioned above, regeneration attempts of Cr(VI)-saturated **MTV-Al-MOF-4** proved ineffective. More specifically, at pH 9, no Cr(VI) desorption was observed, whereas at pH 3, only about 2% of the sorbed Cr(VI) was released. These findings demonstrate that **MTV-Al-MOF-4** cannot regenerate efficiently while maintaining structural integrity following anion capture. Therefore, we propose a post-sorption treatment strategy to enable the recycling of essential organic components, as illustrated in Fig. 8. Specifically, the NH_2-H_2BDC ligand can be

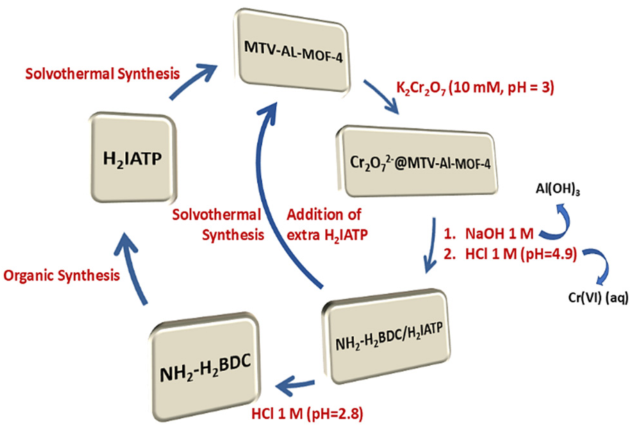

Fig. 8 Recycling process of **MTV-Al-MOF-4**.

recovered in high purity from the oxoanion-loaded framework through a multi-step procedure: (a) treatment of the Cr(VI)-loaded MOF with a NaOH solution, followed by centrifugation to remove the resulting $Al(OH)_3$ precipitate, (b) acidification of the supernatant with HCl solution to approximately pH 5, resulting to precipitation of solid mixture composed of NH_2-H_2BDC and H_2IATP (Fig. S72), (c) subsequent centrifugation and further acidification of the remaining supernatant down to pH ~3, yielding greatly pure (94%) 2-aminoterephthalic acid based on ^1H NMR data (Fig. S73). Details are provided in the SI. It is important to note that Cr(VI) oxoanions remain soluble under alkaline and acidic conditions. This strategy enables the efficient recovery of one of the two organic linkers present in the framework. The recycled 2-aminoterephthalic acid was successfully reused in multiple preparations of 2-(((1*H*-imidazol-4-yl)methyl)amino)terephthalic acid (Fig. 8). Additionally, the recovered ligand mixture (with an $IATP^{2-}/NH_2\text{-}BDC^{2-}$ ratio of 0.75 based on ^1H NMR analysis) was utilized in the synthesis of **MTV-Al-MOF-4** by adding the appropriate amount of H_2IATP to achieve the target 1 : 1 ligand ratio specified in the Experimental section (Fig. 8). These findings highlight the potential to significantly lower material costs and enhance the sustainability of **MTV-Al-MOF**-based sorbents for environmental remediation applications.

2.11 Post-synthetic characterization of Cr(VI)-loaded MOFs-mechanism of anion sorption

Cr(VI)-loaded **MTV-Al-MOF-4** was isolated by treating the activated material with an aqueous solution of $K_2Cr_2O_7$ (pH = 3, 10 mM) (denoted as **$Cr_2O_7^{2-}$@MTV-Al-MOF-4**). PXRD and Le Bail refinement data showed no significant structural differences after Cr(VI) capture (Fig. S74a and S74b). EDS analysis confirmed the presence of Cr(VI) oxoanions (Fig. S75). In addition, the Cl content of the Cr(VI)-loaded material is significantly smaller than that of activated **MTV-Al-MOF-4** (Al : Cl atomic ratio = 17.7 and 38.5 for activated and Cr(VI)-loaded material, respectively). This is consistent with a possible anion exchange involving Cl^- and $Cr_2O_7^{2-}$ anions. FE-SEM images revealed that the MOF particles retained their size and shape after interacting with Cr(VI) (Fig. S76). XPS studies have also been employed to identify the Cr oxidation state and investigate the interactions of the MOF's functional groups with the sorbed ions. As shown in Fig. S77, we can observe the characteristic Cr 2p core-level signals in the anion-loaded material. However, the observed binding energies (576.3 and 578 eV for Cr $2p_{3/2}$ and 585.9 and 587.7 eV for Cr $2p_{1/2}$) do not align with those expected for pure Cr^{6+} or Cr^{3+} oxidation states, but rather indicate the coexistence of mixed Cr^{6+}/Cr^{3+} states. This finding is attributed to the partial reduction of Cr^{6+} induced by X-ray exposure throughout the measurement, a well-established phenomenon in XPS analysis. To determine the oxidation state, we performed magnetic susceptibility measurements at room temperature on the Cr-loaded material. The solid exhibited a diamagnetic response (see SI) which aligns with the presence of Cr^{6+} as the primary species, rather than Cr^{3+} (a paramagnetic ion), confirming that Cr(VI) remains unreduced before the XPS analysis. Moreover, the observed negative shifts in the binding energies of Al 2p, N 1s, and O 1s upon the capture of hexavalent chromium species, although small (approximately ±0.2–0.3 eV), suggest a small electron movement toward the framework (Fig. 9a–c). This finding can be attributed to hydrogen bonding between the Cr–O groups and the Al–OH–Al or –NH groups of the organic backbone, as illustrated by interactions such as Cr–O⋯H–O–Al or Cr–O⋯H–N (Fig. 9d). Gas adsorption measurements indicated that **$Cr_2O_7^{2-}$@MTV-Al-MOF-4** has a BET surface area comparable to the pristine MOF (Fig. S78). Additionally, there were no changes in pore size distribution following Cr(VI) sorption (Fig. S79). It is also important to note that the reported diameter of hydrated $Cr_2O_7^{2-}$ anions is ~6.8 Å;[105] thus, these species cannot enter the pores of the framework (~5.2 Å). This suggests that Cr(VI) oxoanions predominantly interact with the external surface of the MOF particles. Zeta potential analysis has confirmed that the surface of the activated material is positively charged (Fig. S54d). Accordingly, the XPS findings suggest that, in addition to electrostatic interactions, hydrogen bonding also significantly contributes to the strong binding of the oxoanionic species to the MOF. Based on the above, we propose that the dichromate sorption proceeds through an anion-exchange process, and the capturing process is dominated by hydrogen bonding and electrostatic interactions

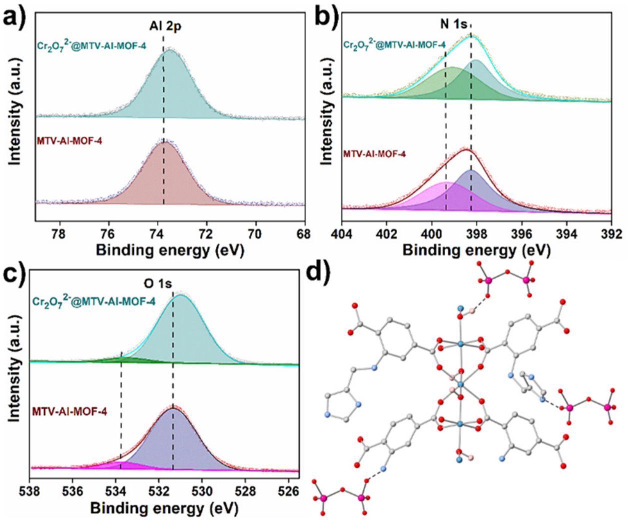

Fig. 9 (a) High resolution Al 2p core-level photoelectron spectra of pristine **MTV-Al-MOF-4** and **$Cr_2O_7^{2-}$@MTV-Al-MOF-4**. The peaks appear at 73.7 and 73.5 eV, respectively. (b) High resolution N 1s core-level photoelectron spectra of pristine **MTV-Al-MOF-4** and **$Cr_2O_7^{2-}$@MTV-Al-MOF-4**. The peaks appear at 398.3/399.3 and 398.0/399.1 eV, respectively. (c) High resolution O 1s core-level photoelectron spectra of pristine **MTV-Al-MOF-4** and **$Cr_2O_7^{2-}$@MTV-Al-MOF-4**. The peaks appear at 531.3/533.7 and 531.0/533.5 eV, respectively. (d) Representation of potential hydrogen bonding interactions (dot lines) between both the amino groups of the dicarboxylate ligands and the OH-groups of the [Al–OH–Al] chains and the oxygen atoms of $Cr_2O_7^{2-}$ (Al, cyan; C, grey; O, red; H, pink; Cr, purple). The structural model was created using Avogadro software.[86]

between the $Cr_2O_7^{2-}$ anions and the **MTV-Al-MOF-4** framework.

2.12. Comparison with other Cr(VI) sorbents in acidic aqueous media

At this stage, it is beneficial to compare the $Cr_2O_7^{2-}$ sorption performance of **MTV-Al-MOF-4** with that of other MOF-based sorbents reported in the literature. Table S2 summarizes primary sorption characteristics, highlighting **MTV-Al-MOF-4** alongside various benchmark MOFs. Remarkably, **MTV-Al-MOF-4** demonstrates a maximum uptake capacity for $Cr_2O_7^{2-}$ comparable to some of the most efficient sorbents, even those with highly porous structures. In addition to its high capacity, this MOF exhibits exceptionally rapid sorption kinetics, achieving equilibrium considerably faster than many state-of-the-art sorbents, typically requiring 10 minutes to 48 hours to reach the equilibrium. Importantly, **MTV-Al-MOF-4** maintains its high sorption efficiency even in the presence of a significant excess of competing ions (Cl^-, NO_3^-, SO_4^{2-}), highlighting its excellent selectivity. MOF-CA composite beads were successfully implemented as the stationary phase in a packed column setup, alongside sea sand, for treating industrial Cr(VI)-contaminated wastewater, marking the first such application reported for an Al(III)-MOF. This highlights the material's substantial potential for practical wastewater decontamination applications.

2.13. Photophysical characterization

The fluorescence properties of all compounds were studied in the solid state upon excitation at 390 nm, after they had been activated through a process of two steps, including solvent exchange with ethanol and protonation with an aqueous HCl solution (*vide supra*). The emission profiles of the presented multivariate MOFs are depicted in Fig. S80. The spectra consist of a broad emission signal between 470–530 nm with a maximum at *ca.* 490 nm. The broad fluorescence band is attributed to the radiative deactivation of the first singlet intraligand excited state, which possesses primarily charge transfer character from the N atom of the secondary amine group to the π^* orbitals of the terephthalate core. The absence of redox activity of the Al(III) centers precludes the contribution of charge transfer transitions involving the metal. An identical, albeit much weaker, emission profile is also observed for the Cr-loaded material **$Cr_2O_7^{2-}$@MTV-Al-MOF-4** (Fig. S81). Similarly, solid-state UV-Vis spectroscopy data show that the absorption profile of **MTV-Al-MOF-4** is noticeably altered after dichromate sorption (Fig. S82). The characteristic absorption peak of Cr(VI) oxoanions ($Cr_2O_7^{2-}$, 350 nm) is not visible due to overlap with the MOF's intrinsic absorption bands. Among the studied compounds, the material with the highest NH_2-BDC content, **MTV-Al-MOF-5**, exhibits the highest fluorescence quantum yield, 9.53% (Fig. S83). This value is almost twice that of the other compounds, which range between 4.64–4.93% (Fig. S84–S87). All results related to the calculated quantum yields and fluorescence lifetimes are summarized in Table 1. In line with its weaker emission signal, Cr-loaded material shows a four-fold decrease in fluorescence quantum yield, down to 1.1% (Fig. S81), thereby confirming that the sorption of $Cr_2O_7^{2-}$ anions causes emission quenching due to electron and/or energy transfer deactivation pathways taking place between the ligand fluorophores and the sorbed Cr(VI) anions.[50,106] The emission lifetimes show a similar trend to the quantum yields, with the chromium-free MOFs showing multiexponential decays with average lifetimes ranging from *ca.* 4.0 to 6.0 ns. In comparison, **$Cr_2O_7^{2-}$@MTV-Al-MOF-4** shows a shorter average decay time of 2.5 ns (Table 1). The fact that the decrease in emission lifetime is not as pronounced as the decrease in quantum yield indicates that the quenching mechanism is primarily static. In this case, the chromophores directly associated with $Cr_2O_7^{2-}$ anions are essentially non-emissive, while those that do not directly interact with guest anions largely exhibit their native emission.[107] The fluorescence results above further support the hypothesis that the sorbed Cr(VI) anions primarily interact with chromophores on the surface of the MOF particles rather than those in the bulk.

We further attempted to perform fluorescence titrations where aliquots of a 10^{-4} M stock aqueous solution of $K_2Cr_2O_7$ at pH 3 were added to a stirred suspension of **MTV-Al-MOF-4** (0.05 mg mL^{-1}) in double distilled water and commercial potable water at pH 2 while recording the MOF's fluorescence signal upon excitation at 390 nm (Fig. S88). Although a quenching trend was observed, it was rather modest, reaching a maximum of approximately 30% loss of initial emission intensity by the end of the study (Fig. S88). These results clearly show that although **MTV-Al-MOF-4** shows promising sorption properties, it does not possess the characteristics of a good fluorescence sensor, which must interact effectively with the targeted analyte at the low concentrations employed in a fluorescence experiment.

Table 1 Collected emission lifetimes and quantum yields of the studied **MTV-Al-MOF** samples

		Fluorescence lifetimes (ns)			
Sample	Φ (%)	τ_1	τ_2	τ_3	$\langle\tau\rangle$
MTV-Al-MOF-1	4.93	0.96(18.8%)	2.92(58.6%)	9.4(22.6%)	4.0
MTV-Al-MOF-2	4.82	0.90(23.0%)	2.85(54.5%)	9.85(22.5%)	4.0
MTV-Al-MOF-3	4.69	0.8(20.9%)	2.72(56.4)	9.62(22.7%)	3.9
MTV-Al-MOF-4	4.64	0.92(26.4%)	2.87(55.6%)	10.51(18.0%)	3.7
MTV-Al-MOF-5	9.53	0.95(21.6%)	3.53(45.0%)	12.58(33.4%)	6.0
$Cr_2O_7^{2-}$@MTV-Al-MOF-4	1.11	0.48(35.9%)	2.11(46.0%)	7.72(18.1%)	2.5

3. Conclusions

In conclusion, five isostructural multivariate Al(III) MOFs (**MTV-Al-MOF-1** to **MTV-Al-MOF-5**) with the MIL-53 structure were isolated *via* solvothermal synthesis. The MOFs demonstrated improved stability in acidic solutions compared to the prototype **NH_2-MIL-53(Al)**, likely due to the presence of bulky –NH–CH_2–Im groups and ultramicropores (~5.2 Å pore size), which hinder the diffusion of reactive species and protect the inorganic backbone of the framework. Gas sorption experiments showed that the **MTV-Al-MOFs** exhibit negligible N_2 adsorption at 77 K but show significant CO_2 uptake even at 273 K. Among them, **MTV-Al-MOF-4** displays the highest CO_2 uptake (2.33 mmol g^{-1}) and exceptional CO_2/N_2 separation performance (~76 at the low-pressure limit), as confirmed by IAST analysis. Detailed batch dichromate sorption studies demonstrated that **MTV-Al-MOF-4** shows rapid sorption properties, with an equilibrium time of less than 5 minutes, and exhibits a relatively high sorption capacity (174 mg g^{-1}), comparable to some highly porous, state-of-the-art MOF-based sorbents. Its Cr(VI) removal efficiency remained exceptional across a wide pH range of 3 to 9. Furthermore, it maintained high performance even with a 10-fold excess of various competitive anions. The sorption process is considered to occur primarily on the external surface of the MOF's particles, as the BET surface area and pore size distribution of the Cr(VI)-saturated MOF are similar to those of the pristine material. The excellent affinity of **MTV-Al-MOF-4** for capturing $Cr_2O_7^{2-}$ is predominantly attributed to strong electrostatic interactions between the positively charged surface of the MOF particles and the Cr(VI) anionic species, along with hydrogen bonds involving $Cr_2O_7^{2-}$ and the –NH_2 or –OH functional groups, as evidenced by XPS data. We also prepared MOF-calcium alginate (CA) beads for a stationary phase in a column setup. In this configuration, the beads, combined with sand, effectively reduced the Cr(VI) concentration in a diluted electroplating wastewater sample to levels within the acceptable drinking water limits. Since direct regeneration of **MTV-Al-MOF-4** was ineffective, we propose a post-sorption strategy to recover the organic components. This method efficiently recycles one of the two organic linkers, enabling the reclaimed NH_2-H_2BDC to be applied in several syntheses of 2-(((1*H*-imidazol-4-yl)methyl)amino)terephthalic acid. Furthermore, the recovered ligand mixture was also utilized to synthesize **MTV-Al-MOF-4**, providing a sustainable approach to reduce material costs in environmental remediation. Fluorescence studies on Cr-free and Cr-loaded **MTV-Al-MOF-4** show that Cr(VI) sorption leads to strong quenching, reducing the fluorescence quantum yield by a factor of four (from 4.6 to 1.1%). The less dramatic decrease in average fluorescence lifetime (from 3.7 to 2.5 ns) indicates a static type of quenching where only a fraction of the ligand fluorophore units directly interacts with the sorbed Cr(VI) anions. This provides further evidence that sorption is predominantly due to electrostatic and/or hydrogen bonding interactions on the surface of MOF particles. Overall, this work presents a flexible synthetic approach to designing MOFs with ultramicroporous structures, enhanced acidic stability, and interesting gas adsorption properties, as well as promising sorption properties for toxic species, such as Cr(IV). Future work will focus on further developing this synthetic strategy, aiming to discover several new multifunctional materials.

Author contributions

Dimitrios A. Evangelou and Eleni C. Makri: investigation, formal analysis, writing – original draft. Nikolaos Pliatsios, Ioannis Vamvasakis, Emilia Buchsteiner, and Panagiotis Oikonomopoulos: investigation, formal analysis. Gerasimos S. Armatas, Giannis S. Papaefstathiou, and Theodore Lazarides: investigation, formal analysis, writing – review & editing, resources. Manolis J. Manos: conceptualization, supervision, resources, writing – original draft.

Conflicts of interest

There are no conflicts to declare.

Data availability

The data supporting this article are provided within the manuscript and the SI: details of synthesis, instrumentation, ^1H NMR, TGA, IR, time-resolved luminescence measurements, gas sorption isotherms, pore size distribution analysis, XPS, PXRD, and Le Bail refinement data, as well as additional data regarding chemical stability studies, desorption studies, and Cr(VI) sorption experiments. See DOI: **https://doi.org/10.1039/d5dt01717c**.

CCDC 2451453 contains the supplementary crystallographic data for this paper.[108]

Acknowledgements

This research has been co-financed by the European Union NextGenerationEU under the call RESEARCH – CREATE – INNOVATE 16971 Recovery and Resilience Facility (project code: TAEDK-06193). We also acknowledge the NMR Centre of the University of Ioannina and the Microscopy Unit of the Chemistry Department of the University of Ioannina for providing facility access.

References

1 T. Rasheed, A. A. Hassan, M. Bilal, T. Hussain and K. Rizwan, *Chemosphere*, 2020, **259**, 127369.
2 X. Guo, Z. Yang, H. Dong, X. Guan, Q. Ren, X. Lv and X. Jin, *Water Res.*, 2016, **88**, 671–680.
3 D. Chen, H. Zhu, S. Yang, N. Li, Q. Xu, H. Li, J. He and J. Lu, *Adv. Mater.*, 2016, **28**, 10443–10458.

4 K. H. Vardhan, P. S. Kumar and R. C. Panda, *J. Mol. Liq.*, 2019, **289**, 111197.

5 C. Femina Carolin, P. Senthil Kumar, A. Saravanan, G. Janet Joshiba and M. Naushad, *J. Environ. Chem. Eng.*, 2017, **5**, 2782–2799.

6 B. Roy, B. Bhunia, T. K. Bandyopadhyay, S. A. Khan, N. B. Nandi and P. C. Nath, in *Handbook of Water Pollution*, Wiley, 2024, pp. 203–226.

7 T. Rasheed, M. Bilal, F. Nabeel, H. M. N. Iqbal, C. Li and Y. Zhou, *Sci. Total Environ.*, 2018, **615**, 476–485.

8 Y. Li, Y. Han and C. Wang, *J. Chem. Eng.*, 2021, **405**, 126648.

9 K. E. Ukhurebor, U. O. Aigbe, R. B. Onyancha, W. Nwankwo, O. A. Osibote, H. Kamdem Paumo, O. M. Ama, C. O. Adetunji and I. U. Siloko, *J. Environ. Manage.*, 2021, **280**, 111809.

10 A. Pratush, A. Kumar and Z. Hu, *Int. Microbiol.*, 2018, **21**, 97–106.

11 P. A. Terry, *Chemosphere*, 2004, **57**, 541–546.

12 M. M. Islam, A. A. Mohana, M. A. Rahman, M. Rahman, R. Naidu and M. M. Rahman, *Toxics*, 2023, **11**, 252.

13 K. Shekhawat, S. Chatterjee and B. Joshi, *Int. J. Adv. Res.*, 2015, **3**, 167–172.

14 M. Valko, H. Morris and M. T. D. Cronin, *Curr. Med. Chem.*, 2005, **12**, 1161–1208.

15 A. Monga, A. B. Fulke and D. Dasgupta, *J. Hazard. Mater. Adv.*, 2022, **7**, 100113.

16 A. Anjum, S. A. Mazari, Z. Hashmi, A. S. Jatoi, R. Abro, A. W. Bhutto, N. M. Mubarak, M. H. Dehghani, R. R. Karri, A. H. Mahvi and S. Nasseri, *Heliyon*, 2023, **9**, e15575.

17 C. Zamora-Ledezma, D. Negrete-Bolagay, F. Figueroa, E. Zamora-Ledezma, M. Ni, F. Alexis and V. H. Guerrero, *Environ. Technol. Innovation*, 2021, **22**, 101504.

18 J. P. Vareda, A. J. M. Valente and L. Durães, *J. Environ. Manage.*, 2019, **246**, 101–118.

19 E. D. Koutsouroubi, I. Vamvasakis, M. G. Minotaki, I. T. Papadas, C. Drivas, S. A. Choulis, G. Kopidakis, S. Kennou and G. S. Armatas, *Appl. Catal., B*, 2021, **297**, 120419.

20 A. L. Taka, K. Pillay and X. Y. Mbianda, *Carbohydr. Polym.*, 2017, **159**, 94–107.

21 H. Liang, B. Song, P. Peng, G. Jiao, X. Yan and D. She, *Chem. Eng. J.*, 2019, **367**, 9–16.

22 S. Horike, S. Shimomura and S. Kitagawa, *Nat. Chem.*, 2009, **1**, 695–704.

23 S. Kitagawa, R. Kitaura and S. Noro, *Angew. Chem., Int. Ed.*, 2004, **43**, 2334–2375.

24 M. Eddaoudi, D. B. Moler, H. Li, B. Chen, T. M. Reineke, M. O'Keeffe and O. M. Yaghi, *Acc. Chem. Res.*, 2001, **34**, 319–330.

25 C. Janiak, *Dalton Trans.*, 2003, **14**, 2781–2804.

26 X. Zhao, X. Yu, X. Wang, S. Lai, Y. Sun and D. Yang, *Chem. Eng. J.*, 2021, **407**, 127221.

27 P. Kumar, A. Pournara, K. H. Kim, V. Bansal, S. Rapti and M. J. Manos, *Prog. Mater. Sci.*, 2017, **86**, 25–74.

28 T. He, Y.-Z. Zhang, X.-J. Kong, J. Yu, X.-L. Lv, Y. Wu, Z.-J. Guo and J.-R. Li, *ACS Appl. Mater. Interfaces*, 2018, **10**, 16172–16180.

29 X. Zhu, B. Li, J. Yang, Y. Li, W. Zhao, J. Shi and J. Gu, *ACS Appl. Mater. Interfaces*, 2015, **7**, 648–655.

30 C. Jeong, M. Z. Ansari, A. H. Anwer, S.-H. Kim, A. Nasar, M. Shoeb and F. Mashkoor, *Sep. Purif. Technol.*, 2023, **305**, 122416.

31 G. Lin, B. Zeng, J. Li, Z. Wang, S. Wang, T. Hu and L. Zhang, *Chem. Eng. J.*, 2023, **460**, 141710.

32 J. Li, X. Wang, G. Zhao, C. Chen, Z. Chai, A. Alsaedi, T. Hayat and X. Wang, *Chem. Soc. Rev.*, 2018, **47**, 2322–2356.

33 G. R. Xu, Z. H. An, K. Xu, Q. Liu, R. Das and H. L. Zhao, *Coord. Chem. Rev.*, 2021, **427**, 213554.

34 L. Rani, J. Kaushal, A. L. Srivastav and P. Mahajan, *Environ. Sci. Pollut. Res.*, 2020, **27**, 44771–44796.

35 U. Habiba, H. H. Ali, S. ur Rehman, A. Khurshid, M. Tahir, S. Ajmal, M. Tabish, M. M. Alam, M. Arif, A. G. Al-Sehemi and G. Yasin, *J. Alloys Compd.*, 2024, **997**, 174785.

36 M. E. Mahmoud, S. M. Elsayed, S. E. Mahmoud, R. O. Aljedaani and M. A. Salam, *J. Mol. Liq.*, 2022, **347**, 118274.

37 Y. Li, T. Huang, X. Liu, Z. Chen, H. Yang and X. Wang, *Sep. Purif. Technol.*, 2023, **314**, 123615.

38 S. Q. Deng, X. J. Mo, S. R. Zheng, X. Jin, Y. Gao, S. L. Cai, J. Fan and W. G. Zhang, *Inorg. Chem.*, 2019, **58**, 2568–2576.

39 L. L. Li, X. Q. Feng, R. P. Han, S. Q. Zang and G. Yang, *J. Hazard. Mater.*, 2017, **321**, 622–628.

40 H. Yang and H. Fei, *Chem. Commun.*, 2017, **53**, 7064–7067.

41 A. V. Desai, B. Manna, A. Karmakar, A. Sahu and S. K. Ghosh, *Angew. Chem., Int. Ed.*, 2016, **55**, 7811–7815.

42 X. Li, H. Xu, F. Kong and R. Wang, *Angew. Chem., Int. Ed.*, 2013, **52**, 13769–13773.

43 P. F. Shi, B. Zhao, G. Xiong, Y. L. Hou and P. Cheng, *Chem. Commun.*, 2012, **48**, 8231–8233.

44 D. Evangelou, A. Pournara, C. Tziasiou, E. Andreou, G. S. Armatas and M. J. Manos, *Inorg. Chem.*, 2022, **61**, 2017–2030.

45 L. Aboutorabi, A. Morsali, E. Tahmasebi and O. Büyükgüngör, *Inorg. Chem.*, 2016, **55**, 5507–5513.

46 A. Nasrollahpour and S. E. Moradi, *Microporous Mesoporous Mater.*, 2017, **243**, 47–55.

47 S. Mukherjee, S. Ghosh and S. Biswas, *ACS Appl. Nano Mater.*, 2023, **6**, 22231–22240.

48 S. Wu, Y. Ge, Y. Wang, X. Chen, F. Li and H. Xuan, *Environ. Technol.*, 2018, **39**, 1937–1948.

49 Z. J. Lin, H. Q. Zheng, H. Y. Zheng, L. P. Lin, Q. Xin and R. Cao, *Inorg. Chem.*, 2017, **56**, 14178–14188.

50 Z. Shao, C. Huang, Q. Wu, Y. Zhao, W. Xu, Y. Liu, J. Dang and H. Hou, *J. Hazard. Mater.*, 2019, **378**, 120719.

51 S. Rapti, D. Sarma, S. A. Diamantis, E. Skliri, G. S. Armatas, A. C. Tsipis, Y. S. Hassan, M. Alkordi, C. D. Malliakas, M. G. Kanatzidis, T. Lazarides,

J. C. Plakatouras and M. J. Manos, *J. Mater. Chem. A*, 2017, **5**, 14707–14719.

52 S. A. A. Razavi and A. Morsali, *Coord. Chem. Rev.*, 2020, **415**, 213299.

53 P. Samanta, S. Let, W. Mandal, S. Dutta and S. K. Ghosh, *Inorg. Chem. Front.*, 2020, **7**, 1801–1821.

54 N. D. Rudd, H. Wang, E. M. A. Fuentes-Fernandez, S. J. Teat, F. Chen, G. Hall, Y. J. Chabal and J. Li, *ACS Appl. Mater. Interfaces*, 2016, **8**, 30294–30303.

55 G.-L. Yang, X.-L. Jiang, H. Xu and B. Zhao, *Small*, 2021, **17**, 2005327.

56 M. E. Mahmoud, Z. Moussa, T. Prakasam, L. Li, M. G. Abiad, D. Patra and M. Hmadeh, *J. Solid State Chem.*, 2020, **281**, 121031.

57 W. P. Lustig, S. Mukherjee, N. D. Rudd, A. V. Desai, J. Li and S. K. Ghosh, *Chem. Soc. Rev.*, 2017, **46**, 3242–3285.

58 S. A. Diamantis, A. Margariti, A. D. Pournara, G. S. Papaefstathiou, M. J. Manos and T. Lazarides, *Inorg. Chem. Front.*, 2018, **5**, 1493–1511.

59 T. K. Pal, *Mater. Chem. Front.*, 2023, **7**, 405–441.

60 L. Fan, D. Zhao, H. Zhang, F. Wang, B. Li, L. Yang, Y. Deng and X. Zhang, *Microporous Mesoporous Mater.*, 2021, **326**, 111396.

61 T. Wiwasuku, J. Boonmak, K. Siriwong, V. Ervithayasuporn and S. Youngme, *Sens. Actuators, B*, 2019, **284**, 403–413.

62 X. Peng, J. Du, J. Fan, J. Wang, Y. Wu, J. Zhao, S. Sun and T. Xu, *J. Am. Chem. Soc.*, 2007, **129**, 1500–1501.

63 T. Wang, E. Lin, Y. L. Peng, Y. Chen, P. Cheng and Z. Zhang, *Coord. Chem. Rev.*, 2020, **423**, 213485.

64 S. Shalini, S. Nandi, A. Justin, R. Maity and R. Vaidhyanathan, *Chem. Commun.*, 2018, **54**, 13472–13490.

65 S. Mukherjee and M. J. Zaworotko, *Trends Chem.*, 2020, **2**, 506–518.

66 S. Nandi, A. Mansouri, I. Dovgaliuk, P. Boullay, G. Patriarche, I. Cornu, P. Florian, G. Mouchaham and C. Serre, *Commun. Chem.*, 2023, **6**, 144.

67 L. Zhao, P. Liu, C. Deng, T. Wang, S. Wang, Y. J. Tian, J. S. Zou, X. C. Wu, Y. Zhang, Y. L. Peng, Z. Zhang and M. J. Zaworotko, *Nano Res.*, 2023, **16**, 12338–12344.

68 B. Liang, X. Zhang, Y. Xie, R. B. Lin, R. Krishna, H. Cui, Z. Li, Y. Shi, H. Wu, W. Zhou and B. Chen, *J. Am. Chem. Soc.*, 2020, **142**, 17795–17801.

69 R. B. Lin, S. Xiang, W. Zhou and B. Chen, *Chem*, 2020, **6**, 337–363.

70 K. J. Chen, H. S. Scott, D. G. Madden, T. Pham, A. Kumar, A. Bajpai, M. Lusi, K. A. Forrest, B. Space, J. J. Perry and M. J. Zaworotko, *Chem*, 2016, **1**, 753–765.

71 R. B. Lin, L. Li, H. L. Zhou, H. Wu, C. He, S. Li, R. Krishna, J. Li, W. Zhou and B. Chen, *Nat. Mater.*, 2018, **17**, 1128–1133.

72 X. Wu, B. Yuan, Z. Bao and S. Deng, *J. Colloid Interface Sci.*, 2014, **430**, 78–84.

73 J. Amaro-Gahete, R. Klee, D. Esquivel, J. R. Ruiz, C. Jiménez-Sanchidrián and F. J. Romero-Salguero, *Ultrason. Sonochem.*, 2019, **50**, 59–66.

74 N. Goel and N. Kumar, *RSC Adv.*, 2018, **8**, 10746–10755.

75 L. Liang, Y. K. Ding, Y. Yin, F. F. Yang and J. Yang, *Chem. Commun.*, 2025, **61**, 1834–1837.

76 W. M. Liao, M. J. Wei, J. T. Mo, P. Y. Fu, Y. N. Fan, M. Pan and C. Y. Su, *Dalton Trans.*, 2019, **48**, 4489–4494.

77 J. Jiao, W. Gong, X. Wu, S. Yang and Y. Cui, *Coord. Chem. Rev.*, 2019, **385**, 174–190.

78 W. Jiang, C. C. Liang and Y. B. Zhang, *Adv. Funct. Mater.*, 2024, **34**, 2308946.

79 Z. Ji, T. Li and O. M. Yaghi, *Science*, 2020, **369**, 674–680.

80 A. Helal, Z. H. Yamani, K. E. Cordova and O. M. Yaghi, *Natl. Sci. Rev.*, 2017, **4**, 296–298.

81 S. J. Lee and S. G. Telfer, *Angew. Chem., Int. Ed.*, 2023, **62**, e202306341.

82 Y. Wei, L. He, Z. Luo, X. Zhou, Z. Zhang, Y. Luo and Q. Liu, *J. Environ. Chem. Eng.*, 2023, **11**, 110436.

83 S. S. Kerur, S. Bandekar, M. S. Hanagadakar, S. S. Nandi, G. M. Ratnamala and P. G. Hegde, *Mater. Today Proc.*, 2021, **42**(Part 2), 1112–1121.

84 A. D. Pournara, S. Rizogianni, D. A. Evangelou, E. K. Andreou, G. S. Armatas and M. J. Manos, *Chem. Commun.*, 2022, **58**, 8862–8865.

85 N. L. Rosi, J. Kim, M. Eddaoudi, B. Chen, M. O'Keeffe and O. M. Yaghi, *J. Am. Chem. Soc.*, 2005, **127**, 1504–1518.

86 *Avogadro: an open-source molecular builder and visualization tool. Version 1.2.0.* https://avogadro.cc/.

87 A. Le Bail, H. Duroy and J. L. Fourquet, *Mater. Res. Bull.*, 1988, **23**, 447–452.

88 A. Le Bail, *Powder Diffr.*, 2005, **20**, 316–326.

89 X. Cheng, A. Zhang, K. Hou, M. Liu, Y. Wang, C. Song, G. Zhang and X. Guo, *Dalton Trans.*, 2013, **42**, 13698–13705.

90 B. Chen, Y. Yang, F. Zapata, G. Qian, Y. Luo, J. Zhang and E. B. Lobkovsky, *Inorg. Chem.*, 2006, **45**, 8882–8886.

91 K. I. Hadjiivanov, D. A. Panayotov, M. Y. Mihaylov, E. Z. Ivanova, K. K. Chakarova, S. M. Andonova and N. L. Drenchev, *Chem. Rev.*, 2021, **121**, 1286–1424.

92 D. K. Sannes, S. Øien-Ødegaard, E. Aunan, A. Nova and U. Olsbye, Quantification of Linker Defects in UiO-Type Metal-Organic Frameworks, *Chem. Mater.*, 2023, **35**, 3793–3800.

93 K. S. Walton and D. S. Sholl, *AIChE J.*, 2015, **61**, 2757–2762.

94 C. Graham, D. A. Imrie and R. E. Raab, *Mol. Phys.*, 1998, **93**, 49–56.

95 M. N. Georgaki, M. Charalambous, N. Kazakis, M. A. Talias, C. Georgakis, T. Papamitsou and C. Mytiglaki, *Environments*, 2023, **10**, 33.

96 J. Wang and X. Guo, *J. Hazard. Mater.*, 2020, **390**, 122156.

97 O. D. Agboola and N. U. Benson, *Front. Environ. Sci.*, 2021, **9**, 678574.

98 D. A. G. Sumalinog, S. C. Capareda and M. D. G. de Luna, *J. Environ. Manage.*, 2018, **210**, 255–262.

99 J. Wang and X. Guo, *Chemosphere*, 2020, **258**, 127279.

100 X. Chen, M. F. Hossain, C. Duan, J. Lu, Y. F. Tsang, M. S. Islam and Y. Zhou, *Chemosphere*, 2022, **307**, 135545.

101 F. Younas, N. K. Niazi, I. Bibi, M. Afzal, K. Hussain, M. Shahid, Z. Aslam, S. Bashir, M. M. Hussain and J. Bundschuh, *J. Hazard. Mater.*, 2022, **422**, 126926.
102 R. Kumar, N. R. Bishnoi, Garima and K. Bishnoi, *Chem. Eng. J.*, 2008, **135**, 202–208.
103 S. Rapti, A. Pournara, D. Sarma, I. T. Papadas, G. S. Armatas, A. C. Tsipis, T. Lazarides, M. G. Kanatzidis and M. J. Manos, *Chem. Sci.*, 2016, **7**, 2427–2436.
104 A. D. Pournara, D. A. Evangelou, C. Roukounaki, E. K. Andreou, G. S. Armatas, T. Lazarides and M. J. Manos, *Dalton Trans.*, 2022, **51**, 17301–17309.
105 Y. Marcus, *Biophys. Chem.*, 1994, **51**, 111–127.
106 D. Sun, W. Liu, M. Qiu, Y. Zhang and Z. Li, *Chem. – Eur. J.*, 2013, **19**, 14279–14285.
107 V. Balzani, P. Ceroni and A. Juris, *Photochemistry and Photophysics: Concepts, Research, Applications*, John Wiley & Sons, 2014.
108 D. A. Evangelou, E. C. Makri, N. Pliatsios, I. Vamvasakis, E. Buchsteiner, P. Oikonomopoulos, G. S. Armatas, G. S. Papaefstathiou, T. Lazarides, M. J. Manos, CCDC 2451453: Experimental Crystal Structure Determination, 2025, DOI: **10.5517/ccdc.csd.cc2n8y41**.